Event Ellipsometer: Event-based Mueller-Matrix Video Imaging

Ryota Maeda[1,2] Yunseong Moon[1] Seung-Hwan Baek[1]
[1]POSTECH [2]University of Hyogo

Abstract

Light-matter interactions modify both the intensity and polarization state of light. Changes in polarization, represented by a Mueller matrix, encode detailed scene information. Existing optical ellipsometers capture Mueller-matrix images; however, they are often limited to capturing static scenes due to long acquisition times. Here, we introduce Event Ellipsometer, a method for acquiring a Mueller-matrix video for dynamic scenes. Our imaging system employs fast-rotating quarter-wave plates (QWPs) in front of a light source and an event camera that asynchronously captures intensity changes induced by the rotating QWPs. We develop an ellipsometric-event image formation model, a calibration method, and an ellipsometric-event reconstruction method. We experimentally demonstrate that Event Ellipsometer enables Mueller-matrix video imaging at 30 fps, extending ellipsometry to dynamic scenes.

1. Introduction

Polarization describes the oscillation of the electric field in light waves, encoding valuable information about the scenes with which light interacts. The polarization state of light can be represented as a Stokes vector $\mathbf{s} \in \mathbb{R}^{4\times1}$ [17]. Polarimetric image analysis focuses on capturing complete or partial forms of the per-pixel Stokes vector and has been extensively studied for shape-from-polarization [31, 36], diffuse-specular separation [19], reflection removal [41], seeing through scattering [42], and transparent object segmentation [32].

Ellipsometry advances polarimetric imaging by analyzing the polarization state of light captured under varying polarization states of illumination. This allows for acquiring polarimetric reflectance, represented as a Mueller matrix $\mathbf{M} \in \mathbb{R}^{4\times4}$ [9], which comprehensively characterizes how light-matter interactions alter the polarization state of incident light. Ellipsometry has been widely used in material science [30, 38], biology [1, 23], and has recently gained attention in computer vision and graphics for 3D shape and reflection analysis [6, 7, 43], material acquisition [8], light transport decomposition [5, 35], and photoelasticity analysis [18].

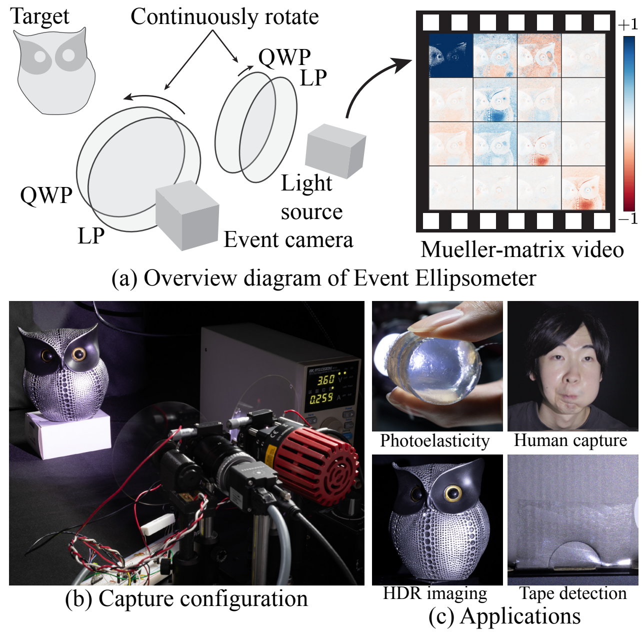

Figure 1. Overview of Event Ellipsometer. (a) Our imaging system captures the Mueller matrix at 30 fps from event streams induced by the continuously rotating QWPs. (b) With our experimental prototype, (c) we demonstrate ellipsometric analysis for dynamic scenes and various applications.

Despite the rich information provided by ellipsometry, its applications have been mainly limited to static scenes because conventional methods require capturing multiple images while mechanically rotating polarizing optics. Typically, more than 20 rotation angles [8] are necessary, leading to long acquisition times and making it impractical for capturing dynamic scenes. Although single-shot Mueller matrix imaging techniques using conventional sensors exist [12, 33, 49], they assume planar target scenes at fixed distances, significantly sacrifice sensor resolution, or use custom-fabricated nano- or micro-optical elements. Additionally, conventional intensity sensors are limited in capturing high-dynamic range (HDR) scenes, often requiring the capture of additional images with multiple exposures.

In this paper, we present *Event Ellipsometer*, a Mueller-matrix imaging method capable of capturing dynamic and HDR scenes. Departing from using conventional intensity sensors, we utilize an event camera, which asynchronously records intensity changes. We equip fast-rotating QWPs and linear polarizers (LPs) in front of both the event camera and an LED light source. The rotating QWPs modulate the polarization state of light emitted and received by the imaging system, resulting in intensity changes captured as events.

We develop an ellipsometric-event image formation model that relates the time differences of adjacent events to the Mueller matrix, normalized by its first element. Using this model, we propose a two-stage Mueller-matrix reconstruction method consisting of per-pixel estimation and spatiotemporal propagation. We incorporate physical validity constraints to handle outliers from sensor noise and scene motion. We also devise calibration methods.

Experimentally, we demonstrate Mueller-matrix imaging at 30 fps, achieving a mean-squared error of 0.045 for materials with known Mueller matrices. Unlike previous single-shot methods [49], Event Ellipsometer can capture non-planar objects and does not compromise spatial resolution. Furthermore, our method is capable of capturing HDR scenes without the need for additional measurement with different exposures.

In summary, our contributions are as follows:

- We propose Event Ellipsometer, enabling Mueller-matrix imaging for dynamic scenes at 30 fps.
- We develop an imaging system using an event camera and a light source, each equipped with synchronized fast-rotating QWPs.
- We formulate an ellipsometric-event image formation model relating event streams to the Mueller matrix, along with a calibration method and a robust ellipsometric-event reconstruction algorithm.
- We experimentally show the high accuracy of Event Ellipsometer on samples with known ground truth, and demonstrate ellipsometric analysis of dynamic scenes with applications on photoelasticity, human capture, HDR imaging, and tape detection.

2. Related Work

Imaging with Polarized Illumination Polarimetric imaging with polarized illumination exploits polarization-dependent light transport to extract material and geometric scene properties. Previous methods often capture scenes with single or a few polarized illuminations and fit parametric models to the captured images [14, 27, 28, 46]. However, this approach is limited by the representation power of the parametric models, thus cannot reveal the true polarimetric reflectance of real-world scenes. Ellipsometry extends polarimetric imaging by directly capturing the Mueller matrix, providing a comprehensive characterization of material polarization properties [4, 17, 20]. It has applications in material science [30, 38], biology [1, 23], and has recently been applied to computer vision and graphics for tasks such as 3D shape analysis [6, 7, 43], material acquisition [8], and light transport decomposition [5, 35]. However, conventional ellipsometry techniques are unsuitable for dynamic scenes because they require capturing multiple images while mechanically rotating polarizing optics and capturing each with an intensity sensor, leading to long acquisition. Single-shot Mueller-matrix imaging methods have been proposed [12, 33, 49], however these approaches often compromise spatial resolution and are limited to planar scenes at fixed distances, restricting their applicability to general dynamic scenes.

Event Cameras for Photometric Analysis Event cameras offer a high temporal resolution of microseconds and a HDR compared to standard frame-based intensity cameras [21]. These advantages have been leveraged for photometric analysis by combining continuously modulated optical light sources or filters. For instance, intensity-modulated illumination with an event camera enables radiance estimation [15, 24] and bispectral photometry [45]. Yu et al. [48] demonstrated event-based photometric stereo for normal estimation with a mechanically-rotating point light source. Hawks et al. [25] and Muglikar et al. [37] explored passive linear-polarization imaging by rotating a linear polarizer in front of an event camera. Existing event-based vision methods cannot capture full polarization reflectance properties as a Mueller-matrix image, limiting their utility.

Imaging with Rotating Optical Elements Rotating optical components have been used for HDR and multispectral imaging [40] and high-speed video reconstruction [13] using a conventional intensity camera. Recently, rotating optics with event cameras have been demonstrated to leverage asynchronous operation and high temporal resolution of the event cameras [25, 26, 37]. These methods rotate optical elements only in front of an event camera without illumination modulation.

3. Imaging System

Experimental Prototype We build an imaging system using an LED light source (Thorlabs MCWHLP3), fast-rotating QWPs (Edmund Optics WP140HE), fixed LPs (Thorlabs WP25M-VIS), and an event camera (Prophesee EVK4). Figure 2(a) and (c) depict our setup, where a pair of a QWP and an LP is placed in front of the event camera and the light source, respectively. We rotate the QWPs so that the event camera detects the event streams caused by the rotating QWPs, from which the normalized Mueller matrix is reconstructed. We can configure the illumination

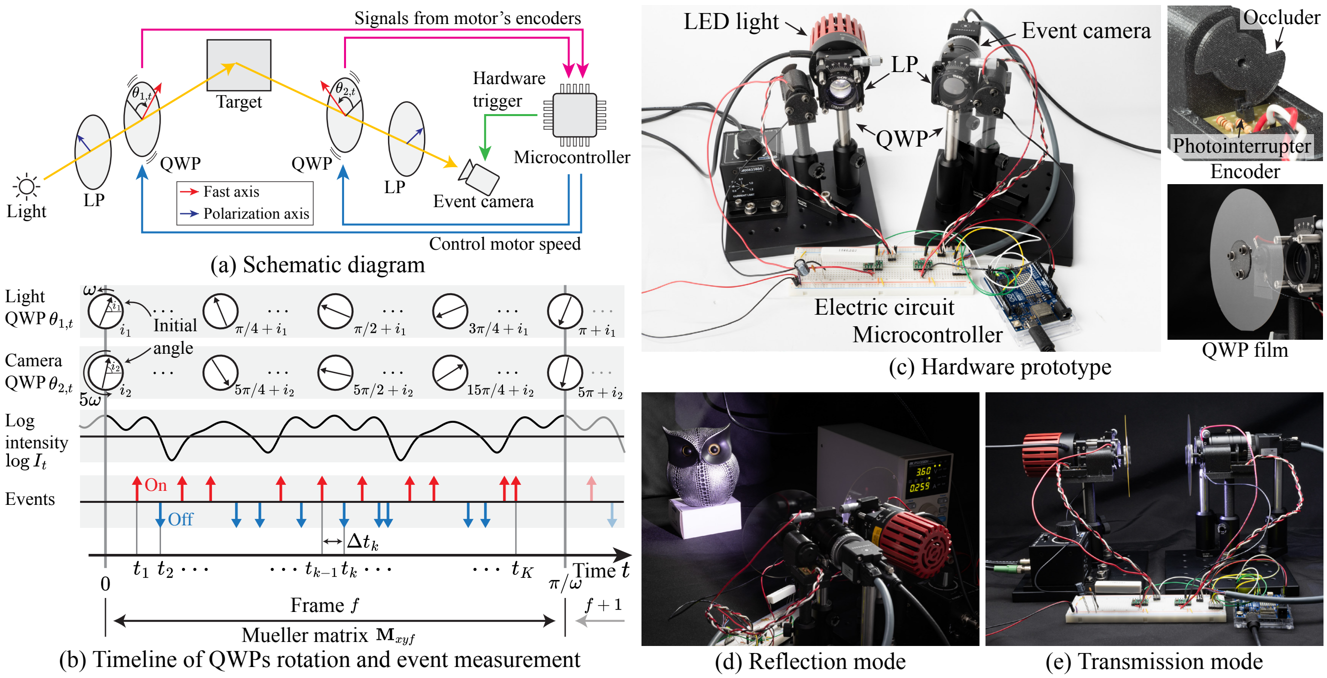

Figure 2. Imaging system of Event Ellipsometer. (a) Schematic diagram illustrating the optical arrangement and hardware operation. (b) Timeline showing the rotation of two QWPs and the event measurement. (c) Our hardware prototype. The system can move the light source and camera position for use in (d) Reflection mode or (e) Transmission mode.

and the camera modules mounted on different breadboards in both the reflection model and the transmission mode as shown in Figure 2(d) and (e). Our system can be seen as a combination of the optical dual rotating retarder [3] and the event-based vision. For a complete list of components, refer to the Supplemental Material.

Rotating QWPs and Angle Encoder We rotate the QWP on the camera side five times faster than the one on the light source side [44]. We denote the QWP angles of the light source and the camera as $\theta_{1,t} = \omega t + i_1, \theta_{2,t} = 5\omega t + i_2$, where $\omega = 30\pi$ rad/sec is the angular velocity of the motor driving the light-source QWP. i_1 and i_2 are the initial QWP angles. One challenge here is to rotate the QWPs at such high speeds while recording their angles $\theta_{1,t}$ and $\theta_{2,t}$ over time t. To this end, we use two independently controlled brushed direct current (DC) motors rotating the QWP films, resulting in an affordable configuration. Also, we develop custom angle encoders using a 3D-printed occluder, a photointerrupter, and an Arduino microcontroller. The occluder rotates at the same speed as the QWP and blocks the light path within the photointerrupter at every π rotation. The microcontroller detects such change at a microsecond resolution and emits a hardware trigger to the event camera. Figure 2(c) shows the angle encoder.

Frame of Mueller Matrix Given the rotation speed of ω, every π rotation of the light-source QWP takes $\pi/\omega \approx$ 33 ms. We set this as the effective temporal duration of each frame f of the Mueller-matrix video which we aim to reconstruct. That is, as shown in Figure 2(b), each frame $f \in \{1, \cdots, F\}$ of the Mueller matrix is estimated based on the events measured during the temporal duration π/ω. F is the number of frames in a reconstructed Mueller-matrix video.

4. Image Formation

Here, we relate the event-camera measurements to the scene Mueller matrix which we aim to reconstruct.

Polarimetric Modulation The LED light source emits unpolarized light of Stokes vector $\mathbf{s} = [1, 0, 0, 0]^\intercal$. At a time t, the light passes through the LP and the QWP rotated by angle $\theta_{1,t}$, resulting in the Stokes vector $\mathbf{Q}(\theta_{1,t})\mathbf{L}(0)\mathbf{s}$, where $\mathbf{Q}(\theta_{1,t})$ and $\mathbf{L}(0)$ denote the Mueller matrices of a QWP rotated by $\theta_{1,t}$ and an LP at 0°, respectively. The light then interacts with the target scene, undergoing polarization change represented by the scene Mueller matrix $\mathbf{M}$. After interaction, the light passes through another QWP at angle $\theta_{2,t}$ and an LP in front of the event camera, resulting in the time-varying intensity I_t incident on the sensor:

$$I_t = [\mathbf{L}(0)\mathbf{Q}(\theta_{2,t})\mathbf{M}\mathbf{Q}(\theta_{1,t})\mathbf{L}(0)\mathbf{s}]_0, \tag{1}$$

where $[\cdot]_0$ denotes intensity, the first element of the Stokes vector.

We rearrange Equation (1) and derive a matrix-vector form:

$$I_t = \mathbf{A}_t \hat{\mathbf{M}}, \tag{2}$$

where $\hat{\mathbf{M}} = [\mathbf{M}_{00}, \mathbf{M}_{01}, \ldots, \mathbf{M}_{33}]^\intercal \in \mathbb{R}^{16\times 1}$ is the vectorized form of $\mathbf{M}$ and $\mathbf{A}_t \in \mathbb{R}^{1\times 16}$ is the system matrix defined as

$$\begin{aligned}\mathbf{A}_t =& [1, \alpha_1^2, \alpha_1\alpha_2, \alpha_2, \alpha_3^2, \alpha_1^2\alpha_3^2, \alpha_1\alpha_2\alpha_3^2, \alpha_2\alpha_3^2,\\ & \alpha_3\alpha_4, \alpha_1^2\alpha_3\alpha_4, \alpha_1\alpha_2\alpha_3\alpha_4, \alpha_2\alpha_3\alpha_4, -\alpha_4\\ & - \alpha_1^2\alpha_4, -\alpha_1\alpha_2\alpha_4, -\alpha_2\alpha_4], \text{where}\\ \alpha_1 =& \cos(2i_1 + 2\omega t), \alpha_2 = \sin(2i_1 + 2\omega t),\\ \alpha_3 =& \cos(2i_2 + 10\omega t), \alpha_4 = \sin(2i_2 + 10\omega t).\end{aligned} \tag{3}$$

For the full derivation, refer to the Supplemental Document.

Differential Intensity The event camera triggers events based on the temporal change of the logarithm of photocurrent [21]. Analytically differentiating the logarithm of Equation (2) with respect to time t, we obtain

$$\frac{\partial \log I_t}{\partial t} = \frac{\frac{\partial I_t}{\partial t}}{I_t} = \frac{\frac{\partial \mathbf{A}_t}{\partial t}\hat{\mathbf{M}}}{\mathbf{A}_t\hat{\mathbf{M}}}, \tag{4}$$

where $\frac{\partial \mathbf{A}_t}{\partial t}$ is given as

$$\begin{aligned}\frac{\partial \mathbf{A}_t}{\partial t} =& [0, -4\alpha_1\alpha_2, 2\alpha_1^2 - 2\alpha_2^2, 2\alpha_1, -20\alpha_3\alpha_4,\\ & - 20\alpha_1^2\alpha_3\alpha_4 - 4\alpha_1\alpha_2\alpha_3^2, 2\alpha_1^2\alpha_3^2 - 20\alpha_1\alpha_2\alpha_3\alpha_4 - 2\alpha_2^2\alpha_3^2,\\ & 2\alpha_1\alpha_3^2 - 20\alpha_2\alpha_3\alpha_4, 10\alpha_3^2 - 10\alpha_4^2,\\ & 10\alpha_1^2\alpha_3^2 - 10\alpha_1^2\alpha_4^2 - 4\alpha_1\alpha_2\alpha_3\alpha_4,\\ & 2\alpha_1^2\alpha_3\alpha_4 + 10\alpha_1\alpha_2\alpha_3^2 - 10\alpha_1\alpha_2\alpha_4^2 - 2\alpha_2^2\alpha_3\alpha_4,\\ & 2\alpha_1\alpha_3\alpha_4 + 10\alpha_2\alpha_3^2 - 10\alpha_2\alpha_4^2, -10\alpha_3, -10\alpha_1^2\alpha_3 + 4\alpha_1\alpha_2\alpha_4,\\ & - 2\alpha_1^2\alpha_4 - 10\alpha_1\alpha_2\alpha_3 + 2\alpha_2^2\alpha_4, -2\alpha_1\alpha_4 - 10\alpha_2\alpha_3].\end{aligned} \tag{5}$$

Events from Polarimetric Modulation For a pixel, we denote the time difference between consecutive events as Δt_k, where $k \in \{1, \cdots, K\}$ is the event index in each frame f. K is the number of detected events at that pixel in the frame f. The time difference is known to be related to the change of photocurrent according to Taylor's expansion [21]:

$$\frac{\partial \log I_{t_k}}{\partial t} = \frac{p_k C}{\Delta t_k}, \tag{6}$$

where event polarity $p_k \in \{+1, -1\}$ is the sign of intensity change, and C is a constant threshold of the event camera.

By combining Equations (4) and (6), we relate the measured per-pixel events to the Mueller matrix, resulting in the image formation model:

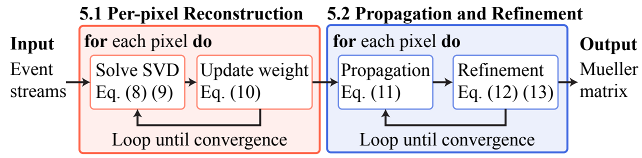

Figure 3. Overview of our Mueller-matrix reconstruction pipeline. This method consists of two steps: (1) per-pixel reconstruction and (2) propagation and refinement.

$$\begin{aligned}\frac{p_k C}{\Delta t_k} &= \frac{\frac{\partial \mathbf{A}_{t_k}}{\partial t_k}\hat{\mathbf{M}}}{\mathbf{A}_{t_k}\hat{\mathbf{M}}}\\ &\Rightarrow \left(\frac{\partial \mathbf{A}_{t_k}}{\partial t_k} - \frac{p_k C}{\Delta t_k}\mathbf{A}_{t_k}\right)\hat{\mathbf{M}} = 0\\ &\Rightarrow \mathbf{B}_{t_k}\hat{\mathbf{M}} = 0,\end{aligned} \tag{7}$$

where $\mathbf{B}_{t_k} \in \mathbb{R}^{1\times 16}$ is the system matrix.

5. Reconstruction

The image formation model in Equation (7) allows us to reconstruct the Mueller matrix $\hat{\mathbf{M}}$. Our reconstruction method, depicted in Figure 3, consists of two main steps: (1) per-pixel reconstruction and (2) spatio-temporal propagation.

5.1. Per-pixel Reconstruction

In this step, our goal is to estimate a Mueller matrix in a computationally efficient manner and being robust to noisy events.

First, we stack the vectors $\mathbf{B}_{t_k}$ for all k, forming a matrix $\mathbf{B} \in \mathbb{R}^{K\times 16}$. We then solve for the vectorized Mueller matrix $\hat{\mathbf{M}}$ by minimizing the weighted least-squares problem:

$$\underset{\hat{\mathbf{M}}}{\text{minimize}} \|\mathbf{WDB}\hat{\mathbf{M}}\|_2^2, \tag{8}$$

where $\mathbf{W} = \text{diag}(\mathbf{w})$ is a diagonal matrix of weights $\mathbf{w} = [w_1, \ldots, w_K] \in \mathbb{R}^{1\times K}$, initialized as ones: $w_k = 1$. The matrix $\mathbf{D} = \text{diag}([\Delta t_1, \ldots, \Delta t_K])$ is a weight matrix that adjusts the influence of each event according to sampling density. This weighting ensures that more densely sampled events at small Δt do not dominate the model fitting. We solve Equation (8) using singular value decomposition (SVD) to obtain $\hat{\mathbf{M}}$ while avoiding the trivial zero solution.

Second, we filter the reconstructed Mueller matrix $\hat{\mathbf{M}}$ to ensure physical validity. Sensor noise and rapid scene dynamics can make solving Equation (8) challenging, often resulting in physically invalid Mueller matrices. These invalid matrices can trap the optimization in local minima. To address this, we apply Cloude's Mueller matrix filtering [16] to project the estimated matrix onto the space of

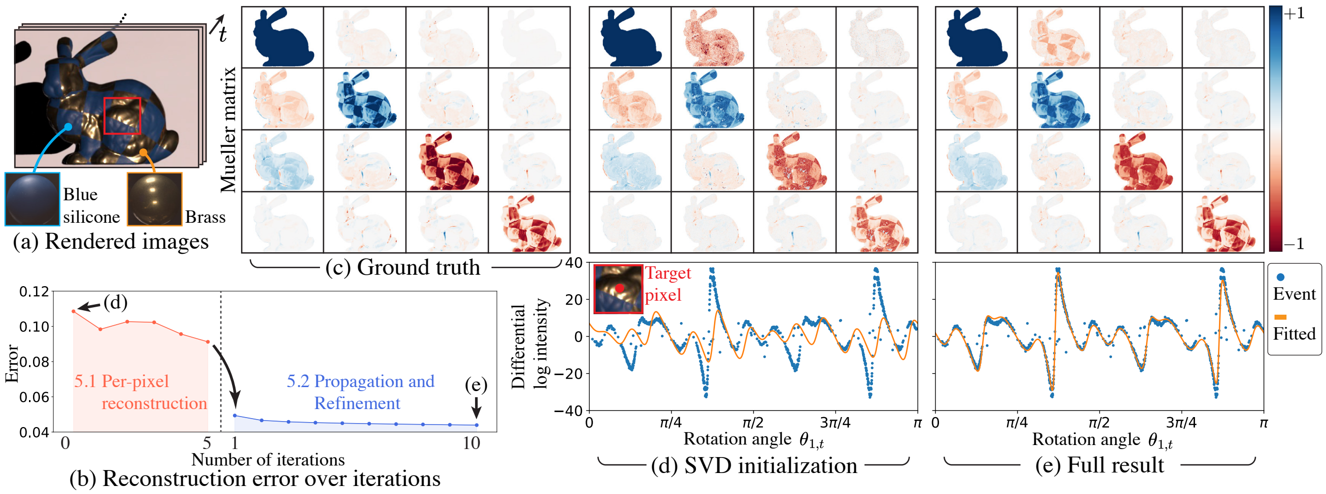

Figure 4. Synthetic data evaluation result. (a) The rendered images include two materials: blue silicone and brass. (b) The plot shows the error (mean absolute error) of the reconstructed Mueller matrix over the number of iterations. (c) Ground truth Mueller matrix. (d)&(e) Top: the reconstructed Mueller-matrix images for the SVD initialization and the full-stage, respectively. Pixels with insufficient event counts are visualized in white. Bottom: a plot of the differentiation of log intensity and fitted line with our method.

physically valid Mueller matrices:

$$\hat{\mathbf{M}} \leftarrow \text{CloudeFilter}(\hat{\mathbf{M}}), \tag{9}$$

where $\text{CloudeFilter}(\cdot)$ denotes the filtering function.

Third, we recalculate the weight vector $\mathbf{w}$ using the physically valid Mueller matrix $\hat{\mathbf{M}}$:

$$w_k = 1/\max(|\mathbf{B}_{t_k}\hat{\mathbf{M}}|, \epsilon), \tag{10}$$

where ϵ is a small positive constant to avoid division by zero sets as 10^{-6} in our experiments. This weight reduces the influence of outlier events and enables robust estimation.

We iterate these three steps—solving the weighted least-squares problem, applying physical validity filtering, and recomputing the weights—until convergence, resulting in the Mueller matrix estimate $\hat{\mathbf{M}}$ for each pixel (x, y) and frame f. We set the maximum number of iterations to 5 in our experiments

5.2. Spatio-temporal Propagation and Refinement

Here, we start by denoting the estimated Mueller matrix at a pixel (x, y) and frame f as $\hat{\mathbf{M}}_{xyf}$ and the corresponding system matrix as $\mathbf{B}_{xyf}$, and weight matrix as $\mathbf{D}_{xyz}$. This second stage refines the Mueller matrix $\hat{\mathbf{M}}_{xyf}$ estimated from the first stage using spatio-temporal neighboring pixels. This process is inspired by PatchMatchStereo from stereoscopic depth estimation [10, 11, 22].

First, we perform propagation. We consider neighboring pixels in both spatial and temporal axes, denoted by $(x', y', f') \in \mathcal{N}(x, y, f)$. The set $\mathcal{N}$ defines a spatio-temporal neighborhood extended from the red-black spatial-only neighborhood [22]. For each pixel at a frame (x, y, f), we update its Mueller matrix if a neighboring pixel (x', y', f') offers a lower error:

$$\begin{aligned}&\hat{\mathbf{M}}_{xyf} \leftarrow \hat{\mathbf{M}}_{x'y'f'},\\ &\text{if} \quad \|\mathbf{D}_{xyz}\mathbf{B}_{xyf}\hat{\mathbf{M}}_{xyf}\|_1 > \|\mathbf{D}_{xyz}\mathbf{B}_{xyf}\hat{\mathbf{M}}_{x'y'f'}\|_1. \end{aligned} \tag{11}$$

Next, we refine the Mueller matrix by applying random perturbations and accepting the perturbation if it reduces the error:

$$\begin{aligned}&\hat{\mathbf{M}}_{xyf} \leftarrow \hat{\mathbf{M}}^{\text{perturb}}_{xyf}, \text{ where}\\ &\hat{\mathbf{M}}^{\text{perturb}}_{xyf} = \text{CloudeFilter}(\hat{\mathbf{M}}_{xyf} \odot (\mathbf{1} + \sigma\mathbf{N})), \qquad (12)\\ &\text{if} \quad \|\mathbf{D}_{xyz}\mathbf{B}_{xyf}\hat{\mathbf{M}}_{xyf}\|_1 > \|\mathbf{D}_{xyz}\mathbf{B}_{xyf}\mathbf{M}^{\text{perturb}}_{xyf}\|_1, \qquad (13)\end{aligned}$$

where $\hat{\mathbf{M}}^{\text{perturb}}_{xyf}$ is the perturbed Mueller matrix, $\odot$ denotes element-wise multiplication, $\mathbf{1}$ is an all-ones matrix, $\mathbf{N} \in \mathbb{R}^{4\times 4}$ contains random values from a standard normal distribution, and σ is a scalar set to 0.01. This multiplicative perturbation preserves the relative scale of the Mueller matrix elements, allowing larger elements to undergo proportionally larger adjustments while smaller elements change minimally. We apply Cloude's filtering to the perturbed Mueller matrix to ensure physical validity.

We repeat the propagation and refinement steps iteratively for a fixed number of iterations set to 10 in our experiments to obtain the final Mueller matrix $\hat{\mathbf{M}}_{xyf}$.

6. Calibration

We perform one-time calibration of the system parameters: contrast threshold (C) and QWP offset angles (i_1 and i_2). Calibration details are provided in the Supplementary Material.

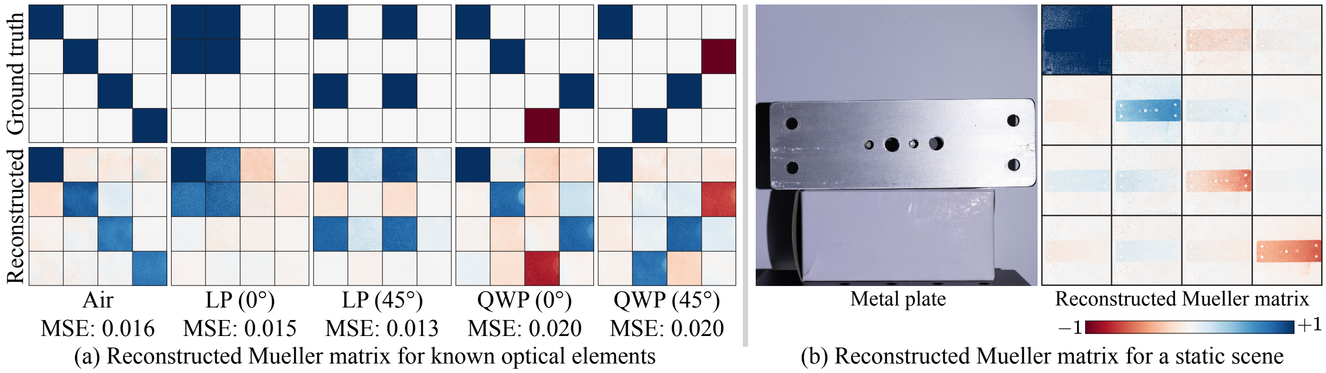

Figure 5. Assessment of reconstructed Mueller matrix on real data. (a) Evaluation with known optical elements. We show the corresponding mean squared errors (MSEs). (b) Measurement on an in-the-wild metal plate induces strong diagonal components.

Contrast Threshold We calibrate the per-pixel contrast threshold C of an event sensor by analyzing pixel responses under controlled illumination stimuli. We increase and decrease the LED intensity linearly over time, and the event camera directly captures the LED light, generating events. We then fit the contrast threshold C to the events per each pixel using Equation (6).

QWP Offset Angle We obtain the offset angles of the fast axis of the QWP in our system: i_1 and i_2 by capturing another QWP sample with known fast axis. Given the known Mueller matrix of the reference QWP, we find the best offset angles that minimize the reconstruction error of Equation (6).

7. Results

Implementation We implemented our reconstruction algorithm in C++ using OpenMP CPU parallelization. It takes 62 seconds for per-pixel reconstruction (Section 5.1), and 68 seconds for the propagation and refinement processes (Section 5.2), measured for processing 500×500-resolution event image sequence of 30 frames, with an average event rate of 153 MEv/s, on the AMD Ryzen 7 7800X3D 8-core processor.

Validation on Synthetic Data To evaluate our method, we render synthetic data in three steps. First, we mimic our capture system by replacing the event camera with an intensity camera in Mitsuba3 [29], and render an image sequence of a synthetic scene for each QWP angle with interval $\omega t = 0.01°$. We use the real-world polarimetric BRDFs to construct the synthetic scene [8]. Then, the rendered images are converted to event streams by simulating event-camera processing based on DVS-Voltmeter [34]. Last, we add Gaussian noise with a standard deviation of 0.5 and replace 5% of true events with values sampled from a Gaussian distribution with a standard deviation of 5.0. Figure 4 shows the synthetic data and reconstructed Mueller matrix using our method. While initial SVD-based estimation suffers from noise with a reconstruction error of 0.11, our full reconstruction improves accuracy with a reconstruction error of 0.04.

Validation on Real Data Figure 5(a) shows that our reconstruction closely matches the corresponding pseudo ground truth of real-world samples: air, linear polarizer (0° and 45°), quarter-wave-plate (0° and 45°). Figure 5(b) shows the result on an in-the-wild sample: a metal plate. The strong diagonal components in this result indicate the preservation of polarization, which is characteristic of reflections from metal surfaces. Notably, these Mueller matrix images are captured in just 33ms, significantly faster than the conventional ellipsometer, which requires several minutes due to its frame-based imaging principle.

Photoelasticity of Transparent Gelatine Photoelasticity is an optical property whereby dielectric materials exhibit birefringence under deformation. Imaging photoelasticity has applications in mechanical stress and material analysis [39, 47]. Analyzing Mueller-matrix images reveals such stress distributions even in transparent objects [18]. Our system enables observing photoelasticity at video rates. Figure 6 shows Mueller-matrix images of a gelatine disk, revealing stress-dependent fringe patterns.

Transparent Tape Detection Detecting transparent objects is challenging for conventional cameras. Sticky tape, a common transparent material used for sealing cardboard, exhibits birefringent properties due to the molecular structure of its stretched plastic. Figure 7 shows the measurement result of sticky tape on a cardboard box. The reconstructed Mueller matrix shows the birefringent property, and we can clearly recognize the tape region. This

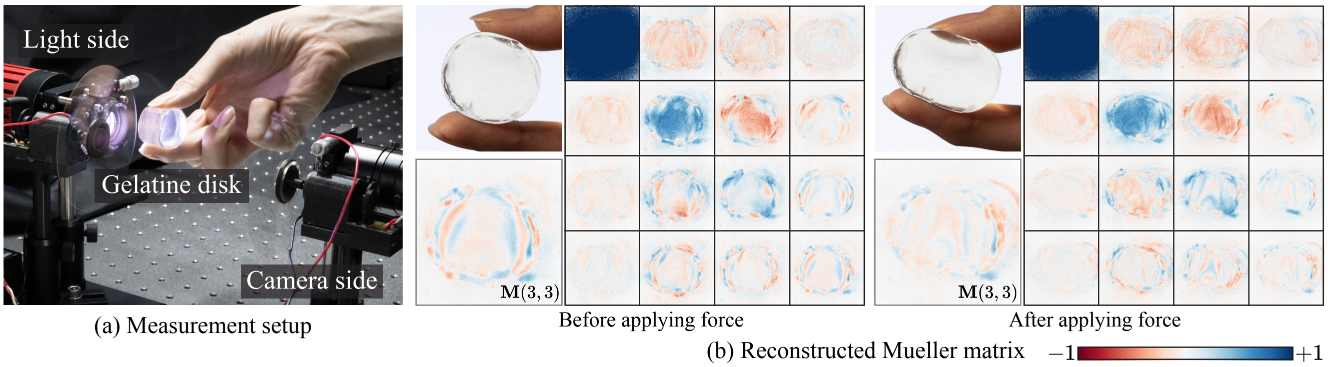

Figure 6. Photoelasticity analysis. (a) Experimental setup for measuring a gelatine disk in transmission mode. We gradually apply force for the gelatine disk to observe changes in photoelastic properties. (b) Reconstructed Mueller matrix images with different forces, revealing complex stress-dependent polarimetric patterns. Notably, as force increases, the Mueller matrix image shows denser fringe patterns.

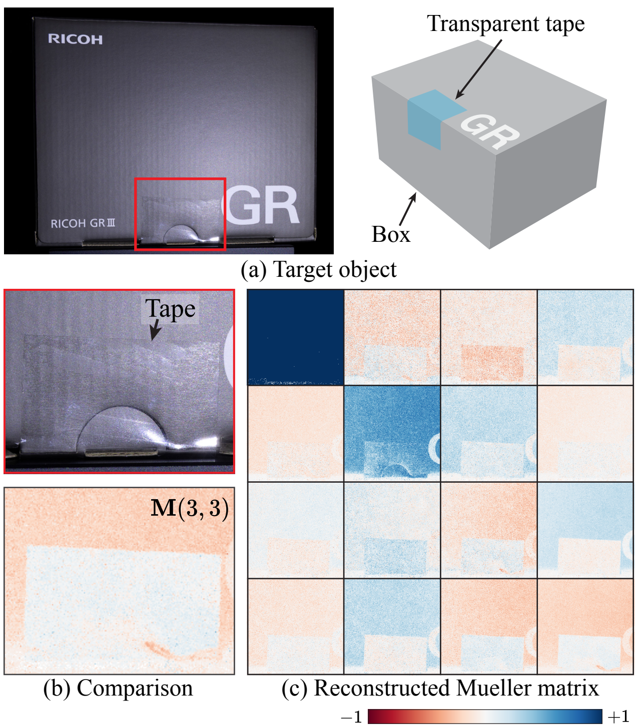

Figure 7. Transparent tape detection. (a) The target object is transparent sticky tape on a box. (b)&(c) The Reconstructed Mueller matrix reveals the tape region, which is difficult to see with a conventional RGB camera.

demonstration shows the potential for inspecting dynamically moving sealed boxes in automated industrial processes.

Dynamic Human Capture Ellipsometers, as a comprehensive polarization imaging technique for human capture, can reveal hidden properties of the human face and hair that are difficult to analyze in conventional imaging and non-ellipsometric polarization imaging [2, 19]. In Figure 8, we demonstrate the Mueller-matrix reconstruction of dynamic facial expressions and hair movements, revealing intricate polarization properties. The reconstructed Mueller matrix for the face exhibits strong diagonal components associated with specular reflection, while the non-diagonal regions display weakly polarized reflection with a dependency on surface normal along the face edges. The hair result shows polarization property in the specular highlight regions.

HDR Mueller-matrix Imaging Our event-based ellipsometer enables Mueller-matrix imaging of HDR scenes. Figure 9 shows reconstruction results on a scene with specular and dark diffuse reflections. While conventional ellipsometers require multiple exposures to prevent overexposure, our method captures the Mueller matrix in HDR scenes at 30 fps without the need for additional measurement.

8. Discussion

Normalized Mueller-Matrix Imaging Normalized Mueller matrix has been extensively used as it provides rich scene information [5, 7, 18]. Since event cameras only detect intensity changes, not intensity itself, our method also reconstructs a normalized version of Mueller matrix per pixel, $\mathbf{M}/\mathbf{M}(0,0)$. We leave reconstructing full Mueller-matrix as a future work that might be accomplished using an event-intensity hybrid imaging system.

End-to-end Real-time Pipeline Although our capture speed is fast, our current Mueller-matrix reconstruction relies solely on CPU acceleration, resulting in a non-real-time pipeline from capture to reconstruction. Implementing GPU acceleration could enable on-the-fly capture, reconstruction, and visualization [22, 48].

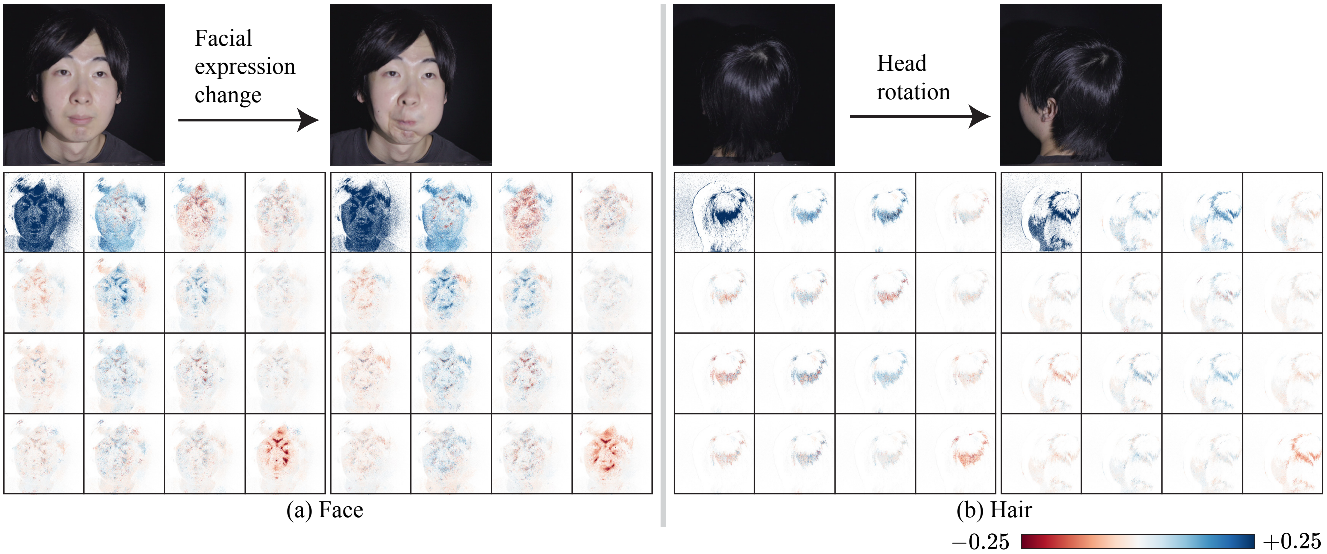

Figure 8. Mueller matrix acquisition for capturing dynamic human (a) face and (b) hair, demonstrating the capture of diffuse and specular polarimetric responses.

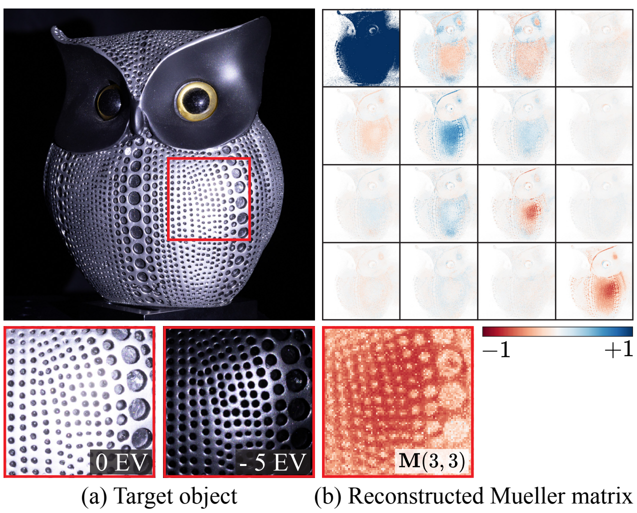

Figure 9. Mueller matrix measurement for a HDR scene. (a) The target scene contains regions with both strong specular reflection and black diffuse reflection. (b) Our proposed method achieves an accurate Mueller-matrix image for the HDR scene in just 33 ms.

Event Bandwidth and Sensitivity The ideal setting of an event camera is to have a low contrast threshold and a short refractory period, to capture subtle intensity changes. However, this produces many events, exceeding the transmission bandwidth, resulting in lost or delayed events [21]. In contrast, when the contrast threshold is high, weakly polarized phenomena cannot be detected as events. Given this trade-off, we defined a region of interest (ROI) in the event sensor and empirically configured the camera settings to find the best parameters.

DC Motor Synchronization For faster rotation speed and precise synchronization between two motors, it is a viable alternative to use brushless DC motors, also known as an electronically commutated (EC) motors. However, this increases system building costs.

Gradient Descent Gradient descent in an automatic differentiation framework offers an alternative approach for Mueller-matrix reconstruction. However, the number of events differs across pixels, which complicates the construction of a dense tensor for efficient computation on modern GPUs.

9. Conclusion

We have introduced Event Ellipsometer, a Mueller-matrix video imaging method that combines an event camera and a light source with fast-rotating QWPs. Our image formation model, calibration, and reconstruction method enable robust Mueller-matrix imaging at 30 fps. We validate our method on synthetic and real data, and demonstrate Mueller-matrix imaging on photoelasticity, dynamic human hair and face capture, HDR imaging, and transparent tape detection.

Acknowledgments Seung-Hwan Baek was supported by Korea NRF (RS-2023-00211658, RS-2024-00438532, 2022R1A6A1A03052954, RS-2024-00437866), and Samsung Research Funding & Incubation Center of Samsung Electronics under Project Number SRFC-IT1801-52.

References

[1] Hans Arwin. Application of ellipsometry techniques to biological materials. *Thin Solid Films*, 519(9):2589–2592, 2011. 1, 2

[2] Dejan Azinović, Olivier Maury, Christophe Hery, Matthias Nießner, and Justus Thies. High-res facial appearance capture from polarized smartphone images. In *Proceedings of the IEEE/CVF Conference on Computer Vision and Pattern Recognition*, pages 16836–16846, 2023. 7

[3] RMA Azzam. Photopolarimetric measurement of the mueller matrix by fourier analysis of a single detected signal. *Optics Letters*, 2(6):148–150, 1978. 3

[4] Rasheed MA Azzam. Stokes-vector and mueller-matrix polarimetry. *JOSA A*, 33(7):1396–1408, 2016. 2

[5] Seung-Hwan Baek and Felix Heide. Polarimetric spatio-temporal light transport probing. *ACM Transactions on Graphics (TOG)*, 40(6):1–18, 2021. 1, 2, 7

[6] Seung-Hwan Baek and Felix Heide. All-photon polarimetric time-of-flight imaging. In *Proceedings of the IEEE/CVF Conference on Computer Vision and Pattern Recognition*, pages 17876–17885, 2022. 1, 2

[7] Seung-Hwan Baek, Daniel S Jeon, Xin Tong, and Min H Kim. Simultaneous acquisition of polarimetric svbrdf and normals. *ACM Trans. Graph.*, 37(6):268, 2018. 1, 2, 7

[8] Seung-Hwan Baek, Tizian Zeltner, Hyunjin Ku, Inseung Hwang, Xin Tong, Wenzel Jakob, and Min H Kim. Image-based acquisition and modeling of polarimetric reflectance. *ACM Trans. Graph.*, 39(4):139, 2020. 1, 2, 6

[9] Seung-Hwan Baek, Ramesh Raskar, Jinwei Ye, Akshat Dave, Achuta Kadambi, and Huaijin Chen. Polarization-based visual computing. In *ACM SIGGRAPH 2023 Courses*, pages 1–1, 2023. 1

[10] Connelly Barnes, Eli Shechtman, Adam Finkelstein, and Dan B Goldman. Patchmatch: A randomized correspondence algorithm for structural image editing. *ACM Trans. Graph.*, 28(3):24, 2009. 5

[11] Michael Bleyer, Christoph Rhemann, and Carsten Rother. Patchmatch stereo-stereo matching with slanted support windows. In *Bmvc*, pages 1–11, 2011. 5

[12] Qizhi Cao, Min Jiang, Chenling Jia, Siyue Jiang, Jing Zhang, Baoli Yao, Mingwu Jin, Edward Dehoog, Lian Duan, Huahua Wang, et al. Snapshot imaging mueller matrix polarimeter using modified savart polariscopes. *Applied Optics*, 62(8):2124–2129, 2023. 1, 2

[13] Dorian Chan, Mark Sheinin, and Matthew O'Toole. Spincam: High-speed imaging via a rotating point-spread function. In *Proceedings of the IEEE/CVF International Conference on Computer Vision*, pages 10789–10799, 2023. 2

[14] Tongbo Chen, Hendrik PA Lensch, Christian Fuchs, and Hans-Peter Seidel. Polarization and phase-shifting for 3d scanning of translucent objects. In *2007 IEEE conference on computer vision and pattern recognition*, pages 1–8. IEEE, 2007. 2

[15] Zehao Chen, Qian Zheng, Peisong Niu, Huajin Tang, and Gang Pan. Indoor lighting estimation using an event camera. In *Proceedings of the IEEE/CVF Conference on Computer Vision and Pattern Recognition*, pages 14760–14770, 2021. 2

[16] Shane R Cloude. Conditions for the physical realisability of matrix operators in polarimetry. In *Polarization Considerations for Optical Systems II*, pages 177–187. SPIE, 1990. 4

[17] Edward Collett. Field guide to polarization. Spie Bellingham, 2005. 1, 2

[18] Akshat Dave, Tianyi Zhang, Aaron Young, Ramesh Raskar, Wolfgang Heidrich, and Ashok Veeraraghavan. Nest: Neural stress tensor tomography by leveraging 3d photoelasticity. *arXiv preprint arXiv:2406.10212*, 2024. 1, 6, 7

[19] Paul Debevec, Tim Hawkins, Chris Tchou, Haarm-Pieter Duiker, Westley Sarokin, and Mark Sagar. Acquiring the reflectance field of a human face. In *Proceedings of the 27th annual conference on Computer graphics and interactive techniques*, pages 145–156, 2000. 1, 7

[20] Hiroyuki Fujiwara. *Spectroscopic ellipsometry: principles and applications*. John Wiley & Sons, 2007. 2

[21] Guillermo Gallego, Tobi Delbrück, Garrick Orchard, Chiara Bartolozzi, Brian Taba, Andrea Censi, Stefan Leutenegger, Andrew J Davison, Jörg Conradt, Kostas Daniilidis, et al. Event-based vision: A survey. *IEEE transactions on pattern analysis and machine intelligence*, 44(1):154–180, 2020. 2, 4, 8

[22] Silvano Galliani, Katrin Lasinger, and Konrad Schindler. Massively parallel multiview stereopsis by surface normal diffusion. In *Proceedings of the IEEE international conference on computer vision*, pages 873–881, 2015. 5, 7

[23] Nirmalya Ghosh and I Alex Vitkin. Tissue polarimetry: concepts, challenges, applications, and outlook. *Journal of biomedical optics*, 16(11):110801–110801, 2011. 1, 2

[24] Jin Han, Yuta Asano, Boxin Shi, Yinqiang Zheng, and Imari Sato. High-fidelity event-radiance recovery via transient event frequency. In *Proceedings of the IEEE/CVF Conference on Computer Vision and Pattern Recognition*, pages 20616–20625, 2023. 2

[25] Michael Hawks and Michael Dexter. Event-based imaging polarimeter. *Optical Engineering*, 61(5):053101–053101, 2022. 2

[26] Botao He, Ze Wang, Yuan Zhou, Jingxi Chen, Chahat Deep Singh, Haojia Li, Yuman Gao, Shaojie Shen, Kaiwei Wang, Yanjun Cao, et al. Microsaccade-inspired event camera for robotics. *Science Robotics*, 9(90):eadj8124, 2024. 2

[27] Inseung Hwang, Daniel S Jeon, Adolfo Munoz, Diego Gutierrez, Xin Tong, and Min H Kim. Sparse ellipsometry: portable acquisition of polarimetric svbrdf and shape with unstructured flash photography. *ACM Transactions on Graphics (TOG)*, 41(4):1–14, 2022. 2

[28] Tomoki Ichikawa, Shohei Nobuhara, and Ko Nishino. Spiders: Structured polarization for invisible depth and reflectance sensing. In *Proceedings of the IEEE/CVF Conference on Computer Vision and Pattern Recognition*, pages 25077–25085, 2024. 2

[29] Wenzel Jakob, Sébastien Speierer, Nicolas Roussel, Merlin Nimier-David, Delio Vicini, Tizian Zeltner, Baptiste Nicolet, Miguel Crespo, Vincent Leroy, and Ziyi Zhang. Mitsuba 3 renderer, 2022. https://mitsuba-renderer.org. 6

[30] GE Jellison, Donovan N Leonard, Lawrence M Anovitz, Chad M Parish, Eliot D Specht, and TM Rosseel. Crystallographic orientation of uniaxial calcite and dolomite determined using reflection generalized ellipsometry. *Journal of Applied Physics*, 124(22), 2018. 1, 2

[31] Achuta Kadambi, Vage Taamazyan, Boxin Shi, and Ramesh Raskar. Polarized 3d: High-quality depth sensing with polarization cues. In *Proceedings of the IEEE international conference on computer vision*, pages 3370–3378, 2015. 1

[32] Agastya Kalra, Vage Taamazyan, Supreeth Krishna Rao, Kartik Venkataraman, Ramesh Raskar, and Achuta Kadambi. Deep polarization cues for transparent object segmentation. In *Proceedings of the IEEE/CVF Conference on Computer Vision and Pattern Recognition*, pages 8602–8611, 2020. 1

[33] Michael W Kudenov, Michael J Escuti, Nathan Hagen, Eustace L Dereniak, and Kazuhiko Oka. Snapshot imaging mueller matrix polarimeter using polarization gratings. *Optics letters*, 37(8):1367–1369, 2012. 1, 2

[34] Songnan Lin, Ye Ma, Zhenhua Guo, and Bihan Wen. Dvs-voltmeter: Stochastic process-based event simulator for dynamic vision sensors. In *European Conference on Computer Vision*, pages 578–593. Springer, 2022. 6

[35] Ryota Maeda and Shinsaku Hiura. Polarimetric light transport analysis for specular inter-reflection. *IEEE Transactions on Computational Imaging*, 10:876–887, 2024. 1, 2

[36] Miyazaki, Tan, Hara, and Ikeuchi. Polarization-based inverse rendering from a single view. In *Proceedings Ninth IEEE International Conference on Computer Vision*, pages 982–987. IEEE, 2003. 1

[37] Manasi Muglikar, Leonard Bauersfeld, Diederik Paul Moeys, and Davide Scaramuzza. Event-based shape from polarization. In *Proceedings of the IEEE/CVF Conference on Computer Vision and Pattern Recognition*, pages 1547–1556, 2023. 2

[38] David A Ramsey and Kenneth C Ludema. The influences of roughness on film thickness measurements by mueller matrix ellipsometry. *Review of scientific instruments*, 65(9):2874–2881, 1994. 1, 2

[39] Michele Scafidi, Giuseppe Pitarresi, Andrea Toscano, Giovanni Petrucci, Sabina Alessi, and Augusto Ajovalasit. Review of photoelastic image analysis applied to structural birefringent materials: glass and polymers. *Optical Engineering*, 54(8):081206–081206, 2015. 6

[40] Yoav Y Schechner and Shree K Nayar. Uncontrolled modulation imaging. In *Proceedings of the 2004 IEEE Computer Society Conference on Computer Vision and Pattern Recognition, 2004. CVPR 2004.*, pages II–II. IEEE, 2004. 2

[41] Yoav Y Schechner, Joseph Shamir, and Nahum Kiryati. Polarization-based decorrelation of transparent layers: The inclination angle of an invisible surface. In *Proceedings of the seventh IEEE international conference on computer vision*, pages 814–819. IEEE, 1999. 1

[42] Yoav Y Schechner, Srinivasa G Narasimhan, and Shree K Nayar. Instant dehazing of images using polarization. In *Proceedings of the 2001 IEEE Computer Society Conference on Computer Vision and Pattern Recognition. CVPR 2001*, pages I–I. IEEE, 2001. 1

[43] Dominik Scheuble, Chenyang Lei, Seung-Hwan Baek, Mario Bijelic, and Felix Heide. Polarization wavefront lidar: Learning large scene reconstruction from polarized wavefronts. In *Proceedings of the IEEE/CVF Conference on Computer Vision and Pattern Recognition*, pages 21241–21250, 2024. 1, 2

[44] Matthew H Smith. Optimization of a dual-rotating-retarder mueller matrix polarimeter. *Applied optics*, 41(13):2488–2493, 2002. 3

[45] Tsuyoshi Takatani, Yuzuha Ito, Ayaka Ebisu, Yinqiang Zheng, and Takahito Aoto. Event-based bispectral photometry using temporally modulated illumination. In *Proceedings of the IEEE/CVF Conference on Computer Vision and Pattern Recognition*, pages 15638–15647, 2021. 2

[46] Tali Treibitz and Yoav Y Schechner. Active polarization descattering. *IEEE transactions on pattern analysis and machine intelligence*, 31(3):385–399, 2008. 2

[47] Li Wang, Yang Ju, Heping Xie, Guowei Ma, Lingtao Mao, and Kexin He. The mechanical and photoelastic properties of 3d printable stress-visualized materials. *Scientific reports*, 7(1):10918, 2017. 6

[48] Bohan Yu, Jieji Ren, Jin Han, Feishi Wang, Jinxiu Liang, and Boxin Shi. Eventps: Real-time photometric stereo using an event camera. In *Proceedings of the IEEE/CVF Conference on Computer Vision and Pattern Recognition*, 2024. 2, 7

[49] Aun Zaidi, Noah A Rubin, Maryna L Meretska, Lisa W Li, Ahmed H Dorrah, Joon-Suh Park, and Federico Capasso. Metasurface-enabled single-shot and complete mueller matrix imaging. *Nature Photonics*, pages 1–9, 2024. 1, 2